Pure & Appl. Chem., Vol. 60, No. 12, pp. 1817–1830, 1988.
Printed in Great Britain.

Nuclear reorganization barriers to electron transfer

Norman Sutin, Bruce S. Brunschwig, Carol Creutz, and Jay R. Winkler

Chemistry Department, Brookhaven National Laboratory, Upton, NY 11973 USA

Abstract - The nuclear barrier to electron transfer arises from the need for reorganization of intramolecular and solvent internuclear distances prior to electron transfer. For reactions with relatively small driving force ("normal" free-energy region) the nuclear factors and rates increase as intrinsic inner-shell and outer-shell barriers decrease; this is illustrated by data for transition metal complexes in their ground electronic states. By contrast, in the inverted free-energy region, rates and nuclear factors decrease with decreasing "intrinsic" barriers; this is illustrated by data for the decay of charge-transfer excited states. Several approaches to the evaluation of the outer-shell barrier are explored in an investigation of the distance dependence of the nuclear factor in intramolecular electron-transfer processes.

One-electron-transfer reactions are at the heart of biological energy transduction and many electrochemical, photochemical, and thermal reaction sequences. For electron transfer between a gaseous atom and its ion, there is no energy barrier to the exchange. However, for the corresponding process in solution or other condensed media, an intrinsic barrier to the exchange develops as a consequence of the radical difference between electron mass (velocity) and that characteristic of the atoms in the molecules surrounding the reaction partners (ref. 1-7); electron motion is many orders of magnitude more rapid than nuclear motion.

For concreteness, consider the transfer of an electron between iron(II) and iron(III) in water depicted in Fig. 1. The six water molecules complexed to the Fe(II) have longer Fe-O distances than those complexed to the Fe(III). In addition, the dipoles of the "outer-shell" water molecules solvating the $Fe(H_2O)_6^{2+}$ and $Fe(H_2O)_6^{3+}$ ions are more strongly oriented in the vicinity of the more highly charged $Fe(H_2O)_6^{3+}$. As is illustrated in Fig. 2, the sudden transfer of an electron from the $Fe(H_2O)_6^{2+}$ to the $Fe(H_2O)_6^{3+}$ (both reactants in their equilibrium configurations) would yield product $Fe(H_2O)_6^{3+}$ and $Fe(H_2O)_6^{2+}$ in non-equilibrium environments. Although such a "vertical" transformation can be accomplished in a photo-induced electron transfer ($h\nu = \lambda$), thermal electron-transfer reactions proceed by a

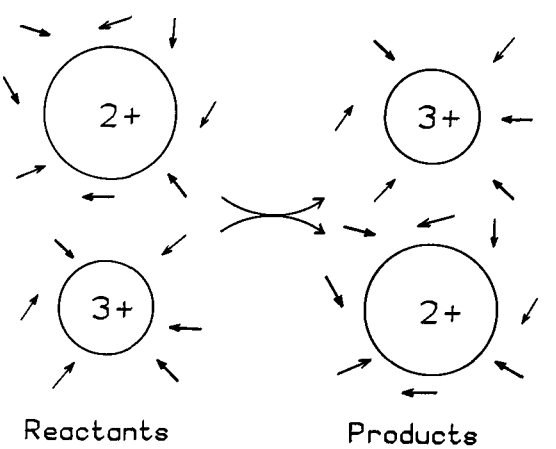

Fig. 1. Illustration of the change in the equilibrium nuclear configurations of the inner-coordination shells of the reactants (represented by the difference in the radii of the oxidized and reduced forms of the redox couple) and the change in the average orientations of the solvent dipoles that result from the transfer of an electron in an exchange reaction.

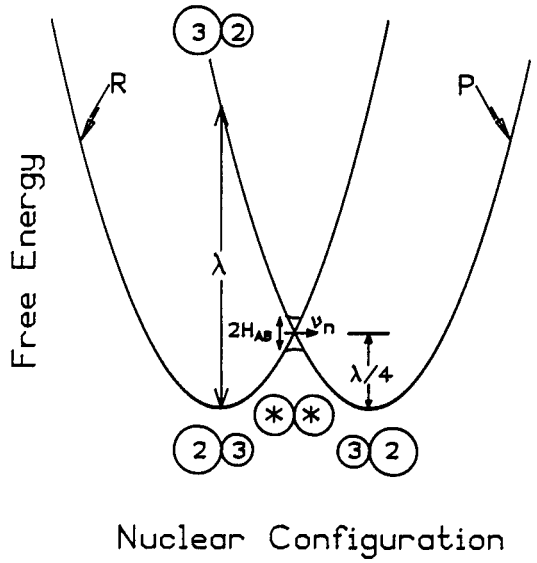

Fig. 2. Plot of the free energy of the reactants (R, left-hand parabola) and products (P, right-hand parabola) as a function of nuclear configuration (reaction coordinate) for an electron-exchange reaction. The splitting at the intersection of the curves is $2H_{AB}$, where H_{AB} is the electronic coupling matrix element. λ is the vertical difference between the free energies of the reactants and products at the equilibrium nuclear configuration of the reactants. Thermal electron transfer occurs at the nuclear configuration appropriate to the intersection of the reactant and product curves.

lower energy path in which inner-shell and outer-shell nuclei rearrange to an intermediate configuration in which the energy of the electron is the same at either redox site. "Sudden" electron transfer can now occur with energy conservation. The requirement for nuclear reorganization prior to thermal electron transfer gives rise to $\Delta G^* = \lambda/4$, the free-energy barrier to the electron exchange. This barrier and its dependence on reactant properties, reactant separation, and the nature of the surrounding medium form the subject of this paper.

Within a semiclassical framework (ref. 4-7), the first-order rate constant k for intramolecular electron transfer between electron donor and acceptor is the product of an electronic transmission coefficient κ_{el}, a nuclear vibration frequency ν_n that takes the activated reactants on to products, and the nuclear factor κ_n:

$$k = \kappa_{el}\, \nu_n\, \kappa_n \quad s^{-1} \qquad (1)$$

(For bimolecular reactions the same framework is applicable once the bimolecular rate constant $k_2(M^{-1}\ s^{-1})$ has been converted to a first-order rate constant by incorporating the stability constant K_A (M^{-1}) for formation of the precursor complex from the separated reactants (ref. 5), i.e. $k_(s^{-1}) = k_2/K_A$. In the applications treated here K_A is evaluated from $K_A = (4\pi N\sigma^2\delta r/1000)\exp[-w(\sigma)/RT]$, where σ is the sum of the van der Waals radii of the two reactants, δr is the range of separation distances over which the rate is appreciable and w is the work required to bring the two reactants together.)

The electron-transfer reaction is adiabatic ($\kappa_{el} \approx 1$) when the probability of activated reactants going on to products is high and nonadiabatic ($\kappa_{el} \ll 1$) when the probability is low. The reaction adiabaticity is determined by the magnitude of the reactant-product electronic coupling H_{AB}; the splitting of the reactant-product "curves" ($2H_{AB}$, see Fig. 2) determines κ_{el}. For nonadiabatic reactions it is convenient to consider the product of the electronic factor κ_{el} and the nuclear vibration frequency ν_n (ref. 4,5):

$$\kappa_{el}\, \nu_n = (2H_{AB}{}^2/h)(\pi^3/\lambda RT)^{1/2} \qquad (2)$$

Provided that the free-energy surfaces are harmonic with identical "reduced" force constants (ref. 4,5), the classical nuclear factor κ_n is given (ref. 1,2,4-7) by eqs 3-5:

$$\kappa_n = \exp(-\Delta G^*/RT) \qquad (3)$$

$$\Delta G^* = (\lambda + \Delta G^\circ)^2/4\lambda \qquad (4)$$

$$\lambda = \lambda_{in} + \lambda_{out} \qquad (5)$$

When the free-energy change for the reaction ΔG° is zero (as in an exchange reaction), $\Delta G^* = \lambda/4$ where λ is comprised of both "fast" inner-shell (λ_{in}) and "slow" outer-shell (λ_{out}) reorganizations (eq 5). For transition metal complexes λ_{in} contains contributions from both metal-ligand and intraligand bond distance and bond angle changes. Designating the reduced and oxidized partners of a redox couple (e.g. $Fe(H_2O)_6^{2+}$ and $Fe(H_2O)_6^{3+}$) as $\underline{2}$ and $\underline{3}$, respectively, the inner-shell reorganization energy for the couple (ref. 4-7) is

$$4\,\Delta G^*_{in} \simeq \lambda_{in} = \frac{1}{2}\sum \bar{f}_i (d^\circ_{\underline{2}} - d^\circ_{\underline{3}})_i^2 \quad ; \quad \bar{f}_i = 2\, f_{\underline{2}} f_{\underline{3}}/(f_{\underline{2}} + f_{\underline{3}}) \qquad (6)$$

where $\bar{f}_i$ is a reduced force constant for the i^{th} inner-shell vibration, $(d^\circ_{\underline{2}} - d^\circ_{\underline{3}})_i = \Delta d^\circ_i$ is the difference in the equilibrium bond distances in the two oxidation states, and the summation is over all the intramolecular vibrations (for the $Fe(H_2O)_6^{2+/3+}$ system, over the 12 metal-ligand bonds if only the breathing motions of the two octahedral reactants are considered). Here a dielectric continuum model (ref. 1,8,9) will be used to evaluate λ_{out}: The medium outside the inner-coordination shells of the reactants is treated as a dielectric continuum with a polarization made up of two parts, a relatively rapid, electronic and a slower, vibrational-orientational polarization. For the special case of two spherical reactants of radius $a_{\underline{2}}$ and $a_{\underline{3}}$ separated (center-to-center) by the distance r ($r > a_{\underline{2}} + a_{\underline{3}}$), λ_{out} is given by eq 7 (ref. 1,8,9) where D_{op} and D_s are, respectively, the optical and static dielectric constants of the bulk solvent. Although eq 7 is only valid when $r > (a_{\underline{2}} + a_{\underline{3}})$, it has often been used for $r \leq (a_{\underline{2}} + a_{\underline{3}})$.

$$\lambda_{out} = (\Delta e)^2 \left(\frac{1}{2a_{\underline{2}}} + \frac{1}{2a_{\underline{3}}} - \frac{1}{r}\right)\left(\frac{1}{D_{op}} - \frac{1}{D_s}\right) \qquad (7)$$

Fig. 3 shows sections through the parabolic basins obtained by plotting the free energies of the reactants and products as a function of the nuclear configuration of their inner- and outer-coordination shells. The straight line joining the R and P minima is the reaction coordinate; this line is the abscissa for the plot in Fig. 2. The dashed line is the path of steepest descent from the activated complex to the R and P minima; this pathway is relevant to the description of the detailed dynamics of the reaction. Evidently the reorganization first occurs along the slower, solvent mode with the contribution from the faster, inner-shell mode increasing as the activated-complex configuration is approached.

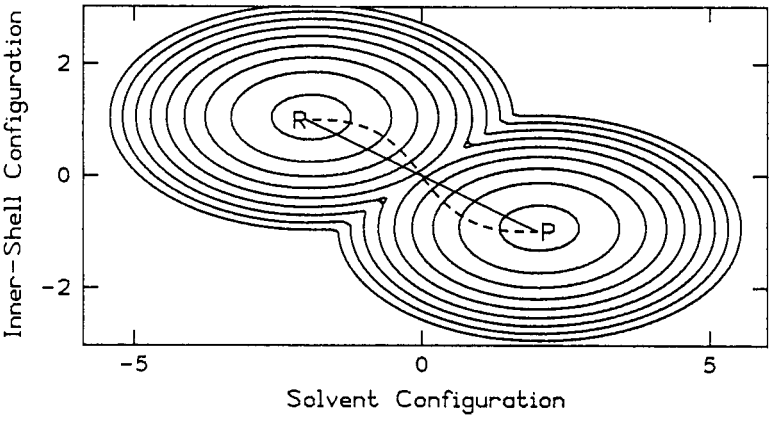

Fig. 3. Sections through the parabolic basins obtained by plotting the free energies of the reactants R and products P in an exchange reaction ($\Delta G^\circ = 0$) as a function of the nuclear configurations in their inner- and outer-shells. A quadratic dependence of the free energy on the nuclear configuration coordinates is assumed. A cut along the straight line joining the R and P minima yields Fig. 2.

FREE-ENERGY REGIMES

In Fig. 2, an exchange reaction was considered. When a driving force or net free-energy change is introduced ($\Delta G^\circ < 0$), the intersection of the reactant and product curves moves to the left (ref. 1-7). In the so-called "normal" free-energy region ($|\Delta G^\circ/\lambda| < 1$), ΔG^* decreases and the nuclear factor increases as the driving force for the reaction becomes more favorable. When $|\Delta G^\circ/\lambda| = 1$ the reaction is barrierless, $\Delta G^* = 0$ and $\kappa_n = 1$. However, when the driving force is increased even further ($|\Delta G^\circ/\lambda| > 1$), the system enters the inverted region; here ΔG^* increases and κ_n decreases with increasing driving force. The profile which emerges when the driving force is increased at constant λ is shown in Fig. 4; the rate and nuclear factors are maximal when $|\Delta G^\circ| = \lambda$ and fall symmetrically at smaller and larger ΔG°.

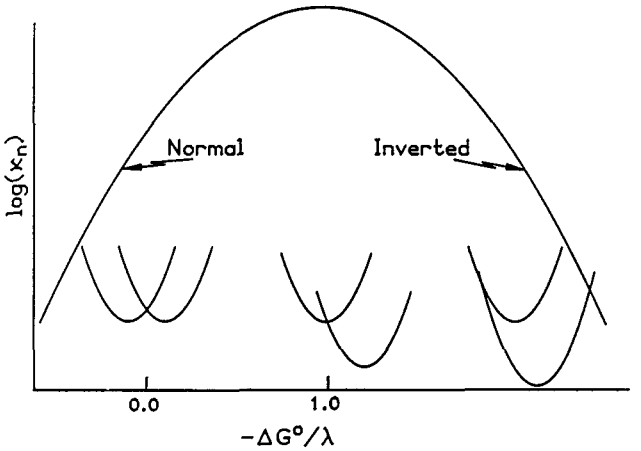

Fig. 4. Variation of the logarithm of the nuclear factor for an electron-transfer reaction with driving force at constant λ. $|\Delta G^\circ/\lambda| < 1$ defines the normal region, $|\Delta G^\circ| = \lambda$ the barrierless region, and $|\Delta G^\circ/\lambda| > 1$, the inverted region.

It is instructive to consider the situation in which ΔG° is held constant and λ is varied (for example, by changing the solvent or the donor-acceptor separation). Again the rate is maximal, $\kappa_n = 1$, when $\lambda = |\Delta G^\circ|$. When $\lambda > |\Delta G^\circ|$, increasing λ decreases κ_n and the rate. By contrast, when $|\Delta G^\circ| > \lambda$, increasing λ increases κ_n and the rate. Thus the nuclear factor responds oppositely to changes in the intrinsic barriers λ_{in} and λ_{out} in the normal and inverted free-energy regions (ref. 1,13-15). Consequently, while diminished reactant separation or solvent polarity promote rapid electron transfer in the normal free-energy region, the opposite is true in the inverted region. This is illustrated in Fig. 5.

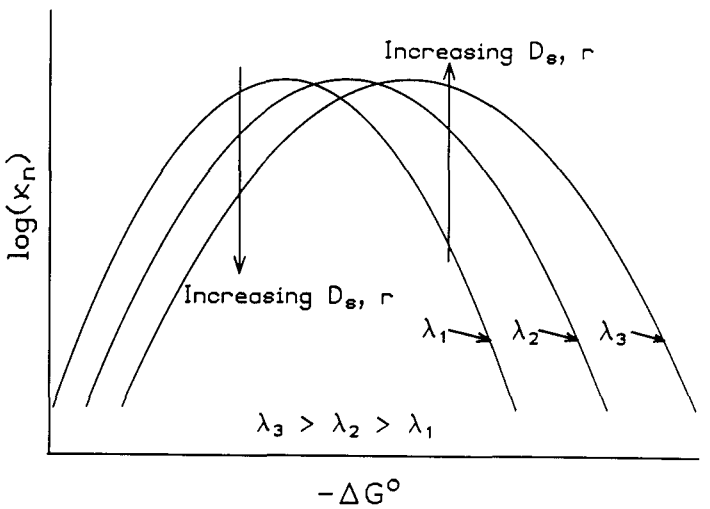

Fig. 5. Illustration of the opposite effects of λ changes on the magnitude of the nuclear factor in the normal and inverted free-energy regions. The λ changes can arise, for example, from changes in "solvent polarity" or donor-acceptor separation (ref. 13-15).

Equations 3-5 are classical expressions; they are valid in the high-temperature limit, i.e., when $h\nu \ll 2kT$ for all of the modes that undergo reorganization. Nuclear tunneling effects are important when $h\nu \gg 2kT$, that is, at low temperature or when a high-frequency mode is involved. Nuclear tunneling corrections are not important for typical exchange reactions at room temperature, and are, in general, small in the normal region. However, such effects can be very large in the inverted region, particularly when high-frequency modes are involved (ref. 3,5-7,10-12), and result in the logarithm of the rate constant depending on the first power of the driving force (energy-gap law of radiationless-transition theory) rather than on the second power predicted by the classical theory.

The organization of the remainder of the article is as follows. First we consider bimolecular exchange reactions ($\Delta G^\circ = 0$). Next we discuss intramolecular electron transfer in bridged systems and metalloproteins (normal region). Finally we consider the spectra and lifetimes of metal-to-ligand charge-transfer excited states (inverted region). The emphasis throughout is on the dependence of λ_{out} on the size and shape of the system and on the distance separating the redox sites.

EVALUATING CONTRIBUTIONS TO THE NUCLEAR FACTOR

Inner-shell barriers

When both structural (X-ray, EXAFS) and vibrational (IR, Raman) data are available for both partners in a redox couple, λ_{in} can be calculated from eq 6. Values obtained for transition metal couples (ref. 16) range from ca. 0 ($Ru(NH_3)_6^{2+/3+}$) to > 2.5 eV ($Co(NH_3)_6^{2+/3+}$). The structures of such complexes are extremely sensitive to population of the metal antibonding σd orbitals, the d-orbitals directed toward the coordinated atoms. A dramatic illustration of this structural sensitivity and the role it plays in determining electron-transfer rates is provided by the polypyridine couples in Table 1.

$$M(bpy)_3^{n+} + M(bpy)_3^{(n+1)+} \longrightarrow M(bpy)_3^{(n+1)+} + M(bpy)_3^{n+} \qquad (8)$$

TABLE 1. Variation of electron self-exchange rate constants (eq 8) with electronic configuration (water, 25 °C; bpy = 2,2'-bipyridine; ref. 17,18).

Couple	d-population	Δd°, Å	k, M^{-1} s^{-1}
(1) $Co(bpy)_3^{2+}/Co(bpy)_3^{3+}$	$(\pi d)^5(\sigma d)^2/(\pi d)^6$	0.19	18
(2) $Co(terpy)_2^{2+}/Co(terpy)_2^{3+}$	$(\pi d)^6(\sigma d)^1/(\pi d)^6$	0.13	3×10^3
(3) $Ni(bpy)_3^{2+}/Ni(bpy)_3^{3+}$	$(\pi d)^6(\sigma d)^2/(\pi d)^6(\sigma d)^1$	0.12	2×10^3
(4) $Co(bpy)_3^{+}/Co(bpy)_3^{2+}$	$(\pi d)^6(\sigma d)^2/(\pi d)^5(\sigma d)^2$	-0.02	1×10^9
(5) $Fe(bpy)_3^{2+}/Fe(bpy)_3^{3+}$	$(\pi d)^6/(\pi d)^5$	0.00	3×10^8
(6) $Ru(bpy)_3^{2+}/Ru(bpy)_3^{3+}$	$(\pi d)^6/(\pi d)^5$	0.00	4×10^8
$Cr(bpy)_3^{2+}/Cr(bpy)_3^{3+}$	$(\pi d)^4/(\pi d)^3$	0.00	2×10^9

Although Δd° varies markedly, correlating with the transfer of an "antibonding" electron in the exchange, the radii of the reactants are essentially constant (because of the relatively large bulk of the bpy or terpy ligand). Thus, assuming the electron exchange occurs at reactant contact, $r = a_2 + a_3 = 2a$, λ_{out} will be constant for the series. Then, provided that κ_{el} does not vary, changes in the self-exchange rate should reflect only variation in λ_{in}. This hypothesis is tested in Fig. 6. Although some deviations from a simple

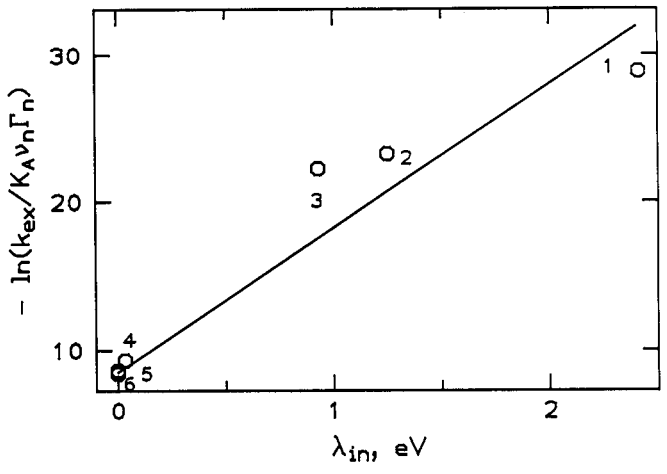

Fig. 6. Plot of $\ln(k_{ex}/K_A\nu_n\Gamma_n)$, where Γ_n is a nuclear tunneling correction, vs λ_{in} for the exchange reactions in Table 1. The numbering corresponds to that used in the table. Changes in bond angles and in intraligand bond distances have been neglected in calculating λ_{in} and the effective mass of a pyridine in the polypyridine was taken as 32. See also ref. 17.

correlation are expected, because only changes in the metal-ligand bond lengths are considered and because κ_{el} may vary, it is evident that the eight orders of magnitude range in rate constants in Table 1 arises predominantly from variations in λ_{in}.

Outer-shell barriers

(1) A two-sphere model in bimolecular reactions. As noted earlier, the two-sphere dielectric continuum model eq 7 has been used widely because of the simplicity (and success) of the expression. Self-exchange reactions for ruthenium(II)/(III) couples have very low inner-shell barriers; for $Ru(NH_3)_6^{2+/3+}$ Δd° = 0.04 Å and for $Ru(bpy)_3^{2+/3+}$ $\Delta d^\circ \approx$ 0.00 Å. The hexaammine and tris(bipyridine) complexes do, however, have very different sizes (a = 3.4 and 6.8 Å, respectively). This suggests that a systematic variation in λ_{out} for ruthenium couples might be achieved by sequentially replacing NH_3 ligands with pyridine or bipyridine ligands (ref. 19). Electron exchange is assumed to occur at van der Waals contact, r = $a_2 + a_3$ = 2a so that eq 7 reduces to $\lambda_{out} \propto 1/(2a)$ when the solvent is held constant. Thus in the $Ru(NH_3)_6$ ... $Ru(bpy)_3$ series, 2a ranges from 6.8 to 13.6 Å; therefore λ_{out} should vary by a factor of 2 and $K_A\kappa_n$ should vary over four orders of magnitude. Figure 7 illustrates how successful this simple treatment can be.

Furthermore, excellent agreement is found between the observed and calculated rate constants:

	k(obsd)	k(calc)
$Ru(NH_3)_6^{2+/3+}$	3.2×10^3	5×10^4 M^{-1} s^{-1}
$Ru(bpy)_3^{2+/3+}$	4.2×10^8	1×10^9 M^{-1} s^{-1}

In this series, the 10^5 variation in exchange rate arises primarily from changing κ_n by manipulation of the radii of the reactants. A limitation of this approach is that the center-to-center separation and the reactant radii cannot be varied independently. This limitation is overcome by turning to binuclear bridged systems in which the length of the bridge can be varied.

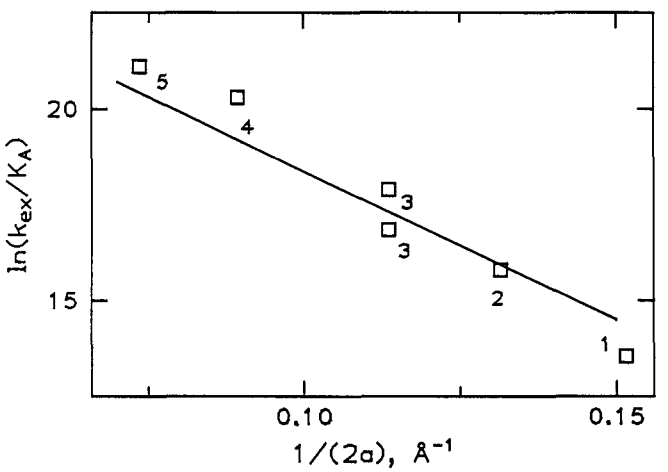

Fig. 7. Plot of $\ell n(k_{ex}/K_A)$ as a function of 1/(2a) for the $Ru(NH_3)_6^{2+/3+}$ ... $Ru(bpy)_3^{2+/3+}$ series; line calculated from eq 7. 1, $(NH_3)_6$; 2, $(NH_3)_5$py; 3, $(NH_3)_4(bpy)$; 4, $(NH_3)_2(bpy)_2$; 5, $(bpy)_3$. (ref. 19)

(2) Intramolecular electron transfer in bridged systems. Applications of an ellipsoidal model. Binuclear bridged systems afford an excellent opportunity to probe the distance dependence of κ_n. In Class II mixed-valence complexes (ref. 20,21) the position (E_{op}) of the metal-to-metal charge transfer (MMCT) transition (eq 9) can be determined as a function of metal-metal separation. Provided that λ_{in} does not vary and that symmetrical bridged systems (ΔG° = 0) are used, the distance dependence of E_{op} should reflect that of λ_{out}.

$$(NH_3)_5Ru^{II}(bridge)Ru^{III}(NH_3)_5 \xrightarrow[E_{op} = \lambda + \Delta G^\circ]{h\nu = E_{op}} [(NH_3)_5Ru^{III}(bridge)Ru^{II}(NH_3)_5]^* \qquad (9)$$

Thermal intramolecular electron-transfer rates can be determined in judiciously designed mixed-metal systems, an approach used by Isied and coworkers (ref. 22,23).

$$(NH_3)_5Os^{II}\text{-iso(proline)}_n\text{-}Ru^{III}(NH_3)_5 \xrightarrow{k} (NH_3)_5Os^{III}\text{-iso(proline)}_n\text{-}Ru^{II}(NH_3)_5 \quad (10)$$

For the mixed-metal systems, ΔG° is not generally zero and κ_{el} is expected to change with r or n. The rate constants thus reflect a complicated set of factors. These may be resolved through studies of the temperature dependences of the rates. The free energy of activation for the electron transfer, deriving from the need for nuclear reorganization, is given by eq 4. The activation energy and entropy associated with the nuclear reorganization can be obtained from the free energy by use of the Gibbs-Helmholtz equation. If λ is assumed to be temperature independent, then ΔH^* and ΔS^* are given by (ref. 24):

$$\Delta H^* = \frac{(\lambda + \Delta H^\circ)^2}{4\lambda} - \frac{(T\Delta S^\circ)^2}{4\lambda} \quad (11a)$$

$$\Delta S^* = \frac{\Delta S^\circ(\lambda + \Delta G^\circ)}{2\lambda} \quad (11b)$$

For eq 10, $\Delta S^\circ \approx 0$ so that $\Delta G^\circ \approx \Delta H^\circ$; also $\Delta S^* \approx 0$ and $\Delta G^* \approx \Delta H^*$. Then, with $k = (k_BT/h)\exp(-\Delta H^{\neq}/RT)\exp(\Delta S^{\neq}/R)$ and $\nu_n \approx k_BT/h$, eq 12 and 13 obtain (ref. 15,22). Thus λ and its distance dependence can be obtained from $\Delta H^{\neq}$ and its distance dependence; κ_{el} can similarly be obtained from $\Delta S^{\neq}$ (ref. 7,24).

$$-\Delta H^{\neq}/RT \approx \ln \kappa_n \approx (\lambda + 2\Delta H^\circ)/4RT \quad (12)$$

$$\Delta S^{\neq}/R \approx \ln \kappa_{el} \quad (13)$$

For the binuclear molecules in eq 9 and 10 an ellipsoidal cavity model appears a more appropriate treatment of the molecular shapes than does the two-sphere model used above. In the ellipsoidal cavity model charge Δe is transferred a distance r along the major axis of an ellipsoidal cavity of internal dielectric constant D_{in}. λ_{out} depends on the shape of the cavity and is quite sensitive to the distance of the redox sites from the surface of the cavity: λ_{out} is relatively large when the cavity surface is highly curved and the redox sites are located near the "ends" of the major axis (ref. 9).

In Fig. 8, the distance dependence of λ_{out} is shown. Generally good agreement between the calculated and experimental values is found. However, the ellipsoidal model used (ref. 9) does tend to overestimate λ_{out} at small r and underestimate λ_{out} at large r. These deviations are believed to arise from specific donor-acceptor interactions between the ammine protons and the solvent and from the fact that, at large r, the ellipsoidal cavity elongates excessively, excluding too much solvent from the vicinity of the redox sites. The latter effect is illustrated in the right-hand side of Fig. 8. In any event, it is evident that λ_{out} increases by more than a factor of 2 over the distance range considered (6-18 Å).

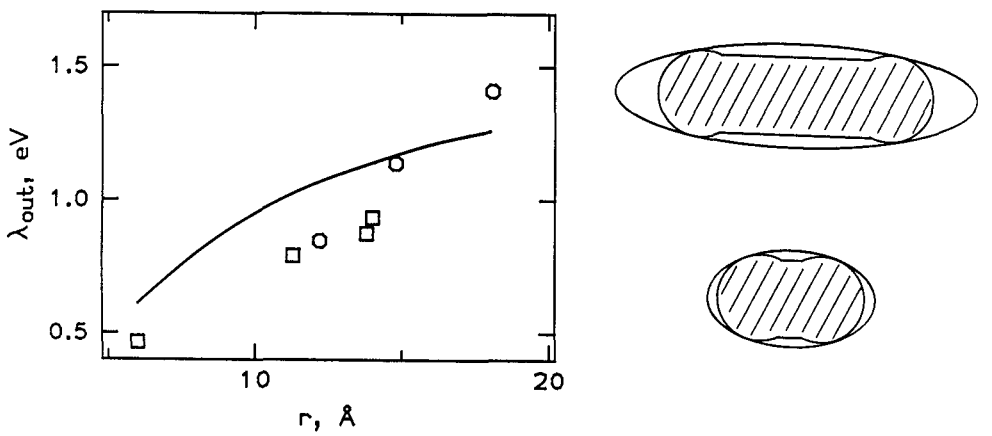

Fig. 8. Left: Distance dependence of λ_{out} (ref. 23). The squares are obtained from MMCT band maxima in water for mixed-valence $[Ru(NH_3)_5]_2L^{5+}$ (L = pyrimidine (6.0 Å) ... 4,4'- bipyridylacetylene (14.0 Å). The circles are obtained from $\Delta H^{\neq}$ for Os(II)-to-Ru(III) electron transfer (eq 10). λ_{out} was obtained from the experimental λ values using $\lambda_{in} = 0.18$ eV; the curve was calculated from the ellipsoidal cavity model (ref. 9). Right: At large separations the ellipsoidal model runs into difficulty because the cavity excludes too much solvent from the vicinity of the charged sites resulting in too low a value of λ_{out} (ref. 9).

Distance dependence of nuclear and electronic factors. The intramolecular electron-transfer rate constants determined for eq 10 are summarized in Table 2.

TABLE 2. Rate constants for intramolecular electron transfer in $(NH_3)_5Os^{II}$-iso(proline)$_n$-$Ru^{III}(NH_3)_5$ at 25 °C (ref. 23).

n	r, Å	k, s^{-1}
0	9.0	$\geq 10^9$
1	12.2	3.1×10^6
2	14.8	3.7×10^4
3	18.1	3.2×10^2
4	21.3	50

The attenuation of electron-transfer rates with separation distance has often been ascribed to the diminution of the electronic factor. When the electronic overlap giving rise to H_{AB} is assumed to decrease exponentially with distance, eq 2 may be approximated as eq 2a (ref. 7)

$$\kappa_{el}\,\nu_n \approx 10^{13}\,\exp[-\beta(r - r_o)] \quad s^{-1} \tag{2a}$$

where the reaction is adiabatic at $r = r_o$, and $\nu_n \approx 10^{13}\ s^{-1}$. Then

$$\Delta S^{\neq}/R = \ln \kappa_{el} = -\beta(r - r_o) \tag{13a}$$

Indeed the data in Table 2 do exhibit an exponential dependence of rate on distance:

$$k = k_o \exp(-\alpha r) \tag{14}$$

However, as shown in Fig. 9, this distance dependence is by no means a consequence of the electronic factor alone: α, the slope of ln k vs r is 1.59 $Å^{-1}$; from the plot of $\Delta S^{\neq}/R$ vs r, β = 0.68 $Å^{-1}$ and from the plot of $\Delta H^{\neq}/RT$ vs r the slope is 0.91 $Å^{-1}$ (ref. 23). Thus the distance dependence of the nuclear factor for the systems in Table 2 is even greater than that of the electronic factor and the assumption that the attenuation of rate with distance arises entirely through the electronic factor can be in serious error.

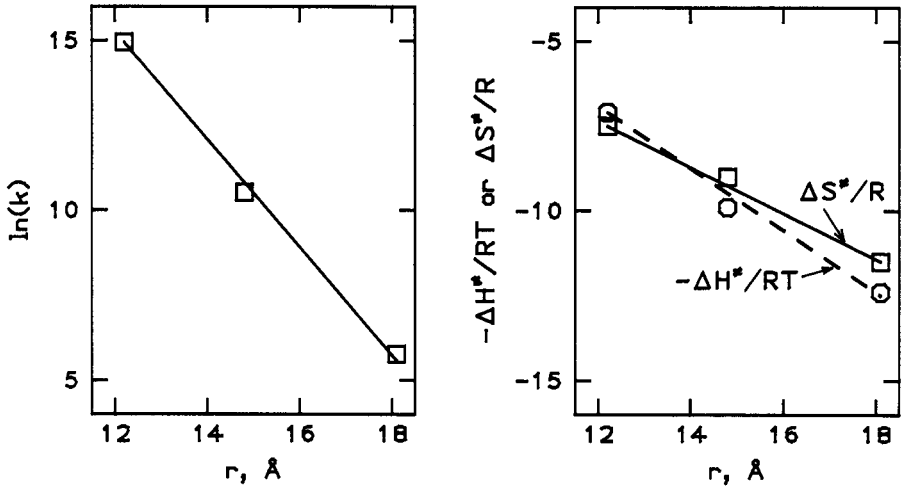

Fig. 9. Distance dependence of the rate constants (left) and activation parameters (right) for intramolecular electron transfer (eq 10) with n = 1 (12.2 Å) ... 3 (18.1 Å). See Table 2 and ref. 23.

(3) A one-sphere model for intramolecular electron transfer. The experimental evaluation of λ_{out} through the investigation of MMCT band energies and through the determination of $\Delta H^{\neq}$ for thermal intramolecular electron transfer was outlined above. A third approach -- the characterization of the dependence of rate on ΔG° for systems with fixed λ -- is considered next; this approach exploits the fact that the electron-transfer rate attains its maximum value when $-\Delta G^{\circ} = \lambda$. For this purpose, the rate is expressed as eq 15 and it is evident that the product $\kappa_{el}\nu_n$ can also be obtained from the maximum rate.

$$k = \kappa_{el}\nu_n \exp[-(\lambda + \Delta G^{\circ})^2/4\lambda RT] \qquad (15)$$

This strategy has been utilized (ref. 25) for electron transfer in "ruthenated" cytochrome *c* derivatives. Cytochrome *c* is a large-radius metalloprotein which normally contains a heme iron. The N-3 of the imidazole group in histidine 33 (≈ 16 Å from the iron) may be used as an attachment point for other metal centers, e.g. $Ru(NH_3)_5^{2+/3+}$ (ref. 26). When the iron is removed from the cytochrome, zinc may be incorporated into the heme site. This substitution introduces a photoactive redox core because the long-lived, porphyrin-centered, singlet and triplet excited states of the Zn derivatives are both powerful oxidizing and reducing agents. Thus, through flash-photolysis studies of the excited-state lifetimes and back-reaction rate constants, a series of intramolecular electron-transfer rate constants may be obtained at constant r (λ_{out}) as a function of ΔG°. To date, the ΔG° range encompassed is > 1 eV and the rate constants range from 2.0 s^{-1} to 3.3 x 10^6 s^{-1}. The data for these systems are shown in Fig. 10.

From Fig. 10 it is concluded that $\kappa_{el}\nu_n = 3.3 \times 10^6$ s^{-1}. Additional studies (ref. 28-30) implicate $\nu_n = 10^{10}$ s^{-1} and $\beta \approx 0.9$ $Å^{-1}$; the latter value is somewhat larger than found for the polypeptide-bridged species in Fig. 9. Interestingly, the value of λ for the cytochrome series, 1.3 eV, is comparable to λ_{out} for the polypeptide-bridged systems at a similar metal-to-metal separation despite the fact that the redox sites are exposed to more solvent in the polypeptide systems.

To model λ_{out} for the derivatized metalloprotein systems a single-sphere model (ref. 31) can be applied. The model appropriate to the cytochrome *c* systems is outlined in Fig. 11 where the calculated dependence of λ_{out} on the location of the $Ru(NH_3)_5$ moiety on the protein surface is also given. For r(M-M) = 18 Å, λ_{out} is calculated to be 0.7 eV, suggesting a significant λ_{in} contribution for the metalloprotein.

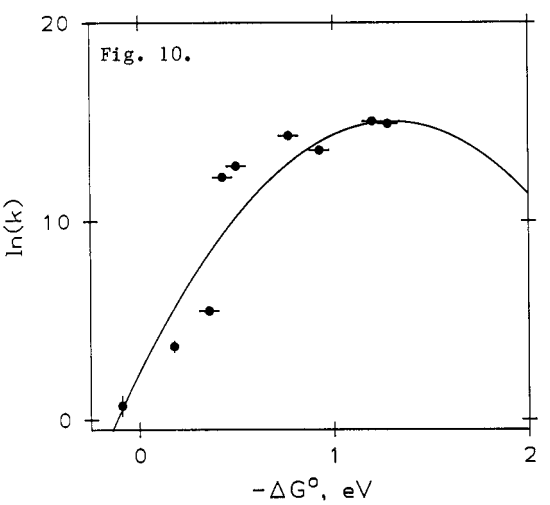

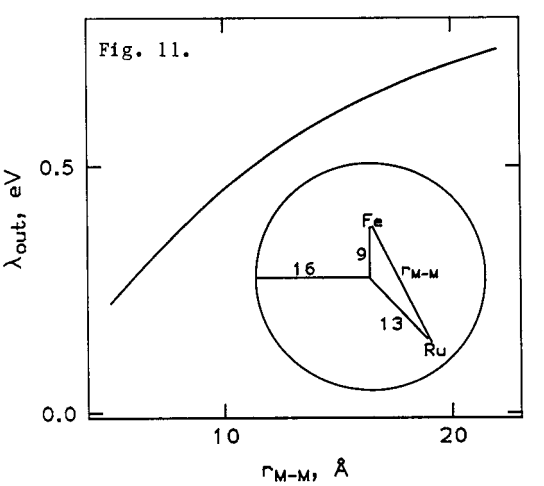

Fig. 10. Dependence of the rate constant for intramolecular electron transfer on driving force for substituted cytochrome *c* derivatives (water, 25 °C). The curve was calculated from eq 15 with $\kappa_{el}\nu_n = 3.3 \times 10^6$ s^{-1} and λ = 1.3 eV. Adapted from ref. 25,27.

Fig. 11. Single-sphere model for intramolecular electron transfer within a derivatized metalloprotein. For the cytochrome *c* derivatives studied in Fig. 10, r(M-M) = 18 Å, the metalloprotein radius is 16 Å (insert) and λ_{out} = 0.7 eV. The curve shows the dependence of λ_{out} on r(M-M) obtained when the ruthenium is moved along the surface of a 13 Å concentric sphere thereby varying r(M-M) from 5 to 22 Å. (In practice, r(M-M) is varied by attaching the $Ru(NH_3)_5$ moiety to different residues on the protein surface, an approach which has been used with myoglobin derivatives (ref. 28).)

Although it has often been assumed that λ_{out} variations can be neglected for metalloprotein systems of this type, it is evident that λ_{out} increases dramatically with the separation of the redox sites. Thus, as for the mixed-valence and polyproline systems, the distance dependence of κ_n (through λ_{out}) must be taken into consideration when interpreting the distance dependence of the electron-transfer rate in metalloprotein systems.

(4) A one-sphere model for charge-transfer band energies - Solvent dependences. It is evident from eq 7 and 13 that the solvent dependence of electron-transfer rates or of MMCT band energies affords another experimental probe of λ_{out} or κ_n. Indeed the solvent dependence of MMCT bands has been rather widely explored for mixed-valence binuclear complexes (ref. 21). The magnitude of λ_{out} is also important in mononuclear systems where knowledge of λ_{out} is vital to understanding absorption/emission spectra and excited-state lifetimes.

The solvent dependences of charge-transfer band maxima reflect the solvent dependences of both $\Delta G°$ and λ. Since, within a dielectric continuum model, $\Delta G°$ is a function of the solvent static dielectric constant D_s while λ_{out} is a function of D_s, D_{op}, and D_{in} (the intra-cavity dielectric constant), the solvent shifts of the band maxima reflect a complicated set of factors. Consequently emissive systems, for which both the sum and difference (Stokes shift) of absorption (E_{abs}) and emission (E_{em}) band maxima can be determined, provide the simplest experimental probes of λ_{out}. For Gaussian-shaped absorption and emission bands (and neglecting zero-point energies) eq 16a and 17a apply (Fig. 12).

$$E_{abs} + E_{em} = 2\Delta G° \tag{16a}$$

$$E_{abs} - E_{em} = 2\lambda = 2(\lambda_{in} + \lambda_{out}) \tag{17a}$$

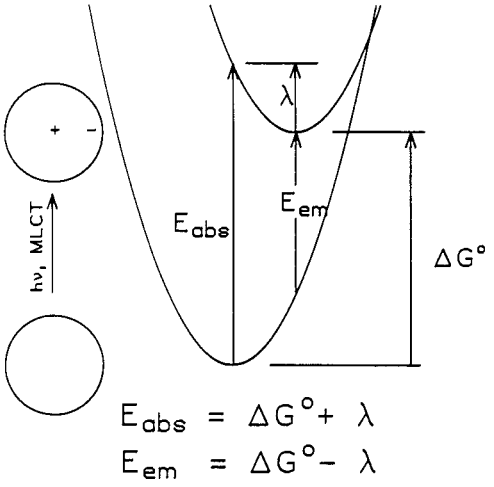

Fig. 12. A classical description of metal-to-ligand charge-transfer (MLCT) absorption and emission. The spherical, non-polar ground-state molecule undergoes MLCT to give a dipolar excited state. Absorption occurs vertically from the ground-state "minimum" and, emission, from the excited-state "minimum". $\Delta G°$ is the free energy of the excited state minus that of the ground state. The ground- and excited-state energy surfaces are assumed to have the same force constants (λ values).

When, as is commonly found in inorganic systems, absorption involves a singlet-singlet transition but emission involves a change in spin-multiplicity ("triplet"-singlet), correction for the singlet-triplet splitting $\Delta(S-T)$ needs to be made and is given by eq 16b, 17b when λ is the same for the singlet and triplet excited states. Here $\Delta G°$ is the energy of the emitting triplet state with respect to the ground (singlet) state.

$$E_{abs}(S\rightarrow S) + E_{em}(T\rightarrow S) = 2\Delta G° + \Delta(S-T) \tag{16b}$$

$$E_{abs}(S\rightarrow S) - E_{em}(T\rightarrow S) = 2\lambda + \Delta(S-T) \tag{17b}$$

Equations 16a–17b are classical expressions. However, when high-frequency modes ($h\nu_{in}$) are present the corrections for zero-point energies can be appreciable, even for Gaussian-shaped bands ($\lambda_{in}/h\nu_{in} > 5$). When $\lambda_{in}/h\nu_{in} \leq 1$ the most intense vibronic component of the absorption or emission band is the zero-zero transition. The energies of these transitions are related by eq 16c and 17c for the case of a classical and a high-frequency mode.

$$E_{abs}(0,0) + E_{em}(0,0) \approx 2\Delta G^\circ + \Delta(S\text{-}T) \tag{16c}$$

$$E_{abs}(0,0) - E_{em}(0,0) \approx 2\lambda_{out} + \Delta(S\text{-}T) \tag{17c}$$

We now turn to a specific example, $Ru(bpy)_3^{2+}$ (ref. 32). For $Ru(bpy)_3^{2+}$, absorption and emission bands are structured as a consequence of the high-frequency intraligand modes ($h\nu_{in} \sim 1350$ cm^{-1}, $\lambda_{in}/h\nu_{in} \approx 1$) (ref. 33). Thus eq 16c and 17c are used. In order to model λ_{out}, $Ru(bpy)_3^{2+}$ is treated as a sphere. For such a symmetric species, the ground state of the molecule has no dipole. However, metal-to-ligand charge-transfer (MLCT) absorption gives rise to a polar excited state when the promoted electron is localized on a single bpy ligand ($[Ru^{III}(bpy)_2(bpy^-)]^{2+}$):

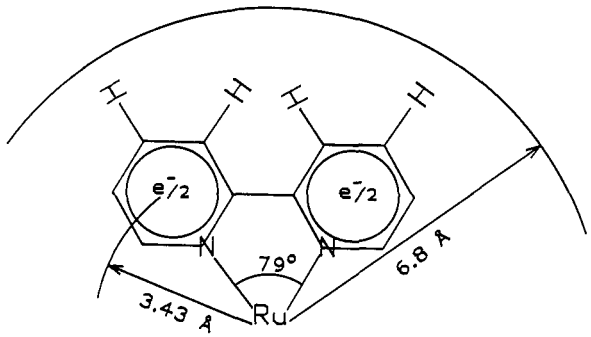

In Fig. 13 the experimental and calculated parameters suggested by eq 16 and 17 are shown. In constructing the plots, $\Delta(S\text{-}T) = 0.58$ eV was used. With the exception of the λ_{out} calculation, only the slopes (solvent shifts) and not the intercepts of the plots are significant because the value of $\Delta(S\text{-}T)$ is uncertain and the value of ΔG° in vacuum (required for the calculation of ΔG° in the various solvents) is not known.

The solvent dependence of the $Ru(bpy)_3^{2+}$ spectra is quite small; this is expected because the charge-transfer distance (3.4 Å) is relatively small and the "cavity" radius (6.8 Å) is relatively large. Despite the small solvent-shift range, good agreement between observed and calculated shifts is found: The experimental values of ($E_{abs} + E_{em}$) and "calculated" $2\Delta G^\circ$ values track the reciprocal of the bulk dielectric constant; the Stokes shifts and calculated λ_{out} values have similar solvent dependences. Note that, while λ_{out} is not a simple function of $1/D_{op} - 1/D_s$ in a general one-sphere model (ref. 31), there is a trend toward increasing λ_{out} at increased $1/D_{op} - 1/D_s$ (increased solvent polarity) in Fig. 13 (right). For $Ru(bpy)_3^{2+}$, it is concluded that $\lambda_{out} \sim 0.095$ eV in water, with

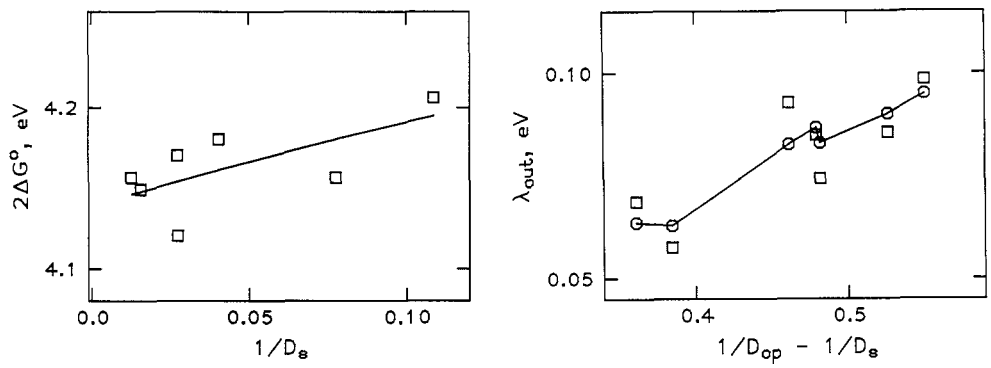

Fig. 13. Comparison of experimental (ref. 33,34) and calculated (spherical cavity, ref. 31) solvent shifts for $Ru(bpy)_3^{2+}$. Left: squares, experimental values of $2\Delta G^\circ$ obtained from eq 16c, and line, calculated values of $2\Delta G^\circ$, plotted vs $1/D_s$. Right: squares, experimental values of λ_{out} obtained from eq 17c, and circles, calculated values of λ_{out}, plotted vs $(1/D_{op} - 1/D_s)$.

λ_{out} being even smaller in most other solvents (0.072 eV in methylene chloride) -- in reasonable agreement with other work (ref. 33-37).

The nuclear factor and excited-state lifetimes. The decay of the $Ru(bpy)_3^{2+}$ MLCT excited state by intramolecular (bpy^- to Ru(III)) electron transfer lies in the inverted region. Therefore the $Ru(bpy)_3^{2+}$ excited-state lifetime in fluid solution should decrease with increasing λ_{out} and decreasing $\Delta G°$ (see Fig. 5). Consistent with this expectation, the excited-state lifetime is shorter in polar than in nonpolar media when intramolecular electron transfer is the only decay route (ref. 33).

When high-frequency inner-shell modes, which give rise to structured spectra, are active the classical rate expression eq 2-5 is inadequate. Instead, expressions derived from radiationless-transition theory are appropriate and have found wide application for MLCT states of a large number of bpy and phen based complexes (ref. 32-37). For the case of a high-frequency mode ($h\nu_{in} \sim 1350\ cm^{-1} \gg 2kT$) and a low-frequency classical mode ($h\nu_{out} \ll 2kT$), the nuclear factor for (nonadiabatic) electron transfer in the inverted region is expressed as eq 18 (ref. 12). (Note eq 18, the two-mode expression for the rate, corresponds to eq 16c and 17c for the MLCT spectrum.)

$$\ell n(\kappa_n) = -\lambda_{in}/h\nu_{in} - \gamma(\Delta G° - \lambda_{out})/h\nu_{in} + [(\gamma + 1)/h\nu_{in}]^2\, \lambda_{out}RT \qquad (18)$$

$$\gamma = \ell n[(\Delta G° - \lambda_{out})/\lambda_{in}] - 1$$

In this limit, classical barrier crossing, even for the relatively slow solvent dipole reorientation ($h\nu_{out}$), ceases to contribute significantly to the rate; instead the low-frequency modes serve to reduce the driving force for electron transfer from $|\Delta G°|$ to $|\Delta G°| - \lambda_{out}$ with the high-frequency mode serving to accept this energy. Thus the dominant high-frequency transition is from the v = 0 level of the initial state to the v' = $(|\Delta G°| - \lambda_{out})/h\nu_{in}$ level of the final state.

The behavior of the nuclear factor in this regime will be illustrated by the series of ruthenium(II) complexes discussed earlier (Fig. 7). Although the Ru(II)/(III) redox potentials vary over almost 1 V, the complexes have similar MLCT absorption maxima (Table 3). Only $Ru(phen)_3^{2+}$ is significantly emissive, but the MLCT states of all of the complexes can be studied by transient absorption spectroscopy. The excited-state lifetimes in this series range from a microsecond to 200 picoseconds, a range of nearly 10,000 in nonradiative decay rate.

TABLE 3. Ground-state MLCT absorption maxima and MLCT excited-state lifetimes in water (25 °C).

Complex	λ_{max}, nm	τ, sec
(1) $Ru(phen)_3^{2+}$	450	1.0×10^{-6} [a]
(2) $Ru(phen)_2(en)^{2+}$	479	2.7×10^{-7} [b]
(3) $Ru(phen)_2(NH_3)_2^{2+}$	482	1.7×10^{-7} [b]
(4) $Ru(phen)(NH_3)_4^{2+}$	471	2.1×10^{-9} [c]
(5) $Ru(pz)(NH_3)_5^{2+}$	471	2.0×10^{-10} [d]

[a]ref. 33. [b]ref. 36. [c]ref. 38. [d]ref. 39.

Empirically, the excited-state lifetimes or nonradiative rate constants correlate with the bimolecular electron-exchange rates in Fig. 7, with the molecular volumes of the complexes, and with the metal-centered redox potentials. The correlation of lifetime with volume suggests that the rate variations may be related to variations of λ_{out} with the "size" of the complex while the correlation with redox potential suggests a systematic variation in $\Delta G°$. To explore the origin of these patterns we turn to eq 18. Because emission data are not available for the tetra- and pentaammine complexes, we use the absorption data alone: $E_{abs} = \Delta G° - \lambda_{out} - \Delta(S\text{-}T)$ (i.e., $\lambda_{in}/h\nu_{in} \leq 1$ is assumed for all of the complexes). In addition we use a simplified treatment suggested by eq 18: For a homologous series of complexes (ref. 33) such as those in Table 3, $\kappa_{el}\nu_n$ and the first and last terms in $\ell n(\kappa_n)$ eq 18 are expected to vary less than the central, "effective energy gap", term. Thus eq 19 is suggested.

$$\ell n(k,obsd) \propto \gamma[E_{abs} - 2\lambda_{out} - \Delta(S\text{-}T)]/h\nu_{in} \qquad (19)$$

E_{abs} and $\ell n(k,obsd)$ are obtained from Table 3; $\Delta(S\text{-}T)$ is taken as a constant (0.58 eV); changes in λ_{in}, $h\nu_{in}$, and γ are neglected, and λ_{out} is obtained from model calculations. [For $Ru(phen)_2(en)^{2+}$, $Ru(phen)_2(NH_3)_2^{2+}$, and $Ru(phen)(NH_3)_4^{2+}$, λ_{out} is

calculated from the averaged spherical radius (6.00, 5.80, 4.62 Å) approximation (ref. 19), with the positions and lengths of the excited-state dipoles being intermediate between the values for $Ru(phen)_3^{2+}$ and $Ru(NH_3)_5pz^{2+}$. For $Ru(NH_3)_5pz^{2+}$, λ_{out} was estimated from band-width considerations (ref. 39).] In Fig. 14, the measured nonradiative decay rates are plotted against the calculated energy gaps.

Fig. 14.

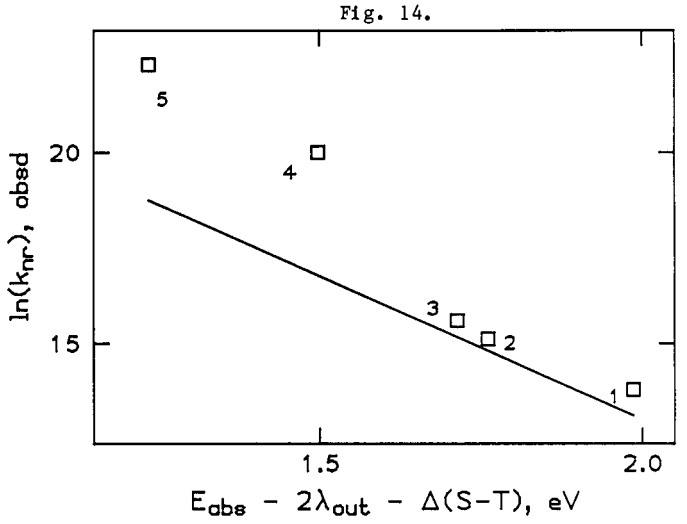

Fig. 15.

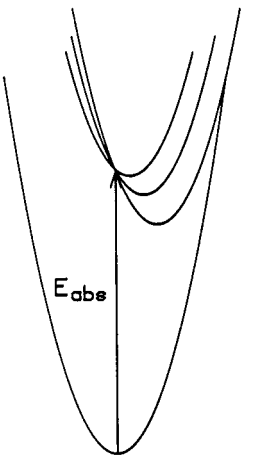

Fig. 14. Plot of the observed rate constants for the nonradiative decay of the MLCT states of the Ru(II) complexes in Table 3 vs $[E_{abs} - 2\lambda_{out} - \Delta(S-T)]$, the effective energy gap for Ru(III)-L^- to Ru(II)-L electron transfer. The line has a slope of 7.49 $(eV)^{-1}$ and intercept 28 (values implicated for $Ru(bpy)_2$-derivatives in ref. 33) and is included as a qualitative comparison.

Fig. 15. Ground- and excited-state manifolds for singlet MLCT states showing the effect of increasing λ_{out} at constant E_{abs}. The triplet excited states are displaced below the corresponding singlet states by a constant amount.

From Fig. 14 it is evident that the Ru(II) MLCT state lifetimes correlate qualitatively with the estimated effective energy-gap values. The line is calculated from parameters (ref. 33) obtained from plots of $\ell n(k,obsd)$ vs E_{em} for $Ru(bpy)_2L_2^{2+}$ derivatives in dichloromethane at 200 K; because of the very different experimental conditions and data treatment it provides only a very qualitative basis for comparison. Surprisingly, however, the $Ru(phen)_3$ and $Ru(phen)_2$ data points fall quite close to the line while the $Ru(NH_3)_4$ and $Ru(NH_3)_5$ rates are only about 30 times "too large". The agreement is especially striking since we have used only absorption data here. Moreover the rate and energy-gap range encompassed is much greater in Fig. 14 than in ref. 33.

While the application of the full eq 18 (or more complex treatments, including intermediate-frequency modes and ligand-field states) would be desirable (but impractical without detailed emission data sets for all of the complexes) the trend in Fig. 14 provides a semiquantitative explanation for the lifetime-size correlation: Although the absorption maxima (E_{abs} values) for the complexes are similar, λ_{out} increases and $\Delta G°$ decreases with increasing number of NH_3 groups; thus $\Delta G° - \lambda_{out}$ drops along the series and the intramolecular electron-transfer rates increase. Here the approximate constancy of E_{abs} reflects opposing changes in $\Delta G°$ and λ_{out} (Fig. 15). Thus E_{abs} alone does not determine excited-state lifetime (and photoreactivity): At the one extreme, $Ru(phen)_3^{2+}$, the long excited-state lifetime makes possible a rich bimolecular excited-state photochemistry; at the other, the very short-lived $Ru(NH_3)_5pz^{2+}$, the only bimolecular photochemistry detected involves reactions with the solvent.

CONCLUDING REMARKS

The sources and consequences of variations in the nuclear factor in electron-transfer reactions have been examined. In transition metal systems, variations of the inner-shell barrier with σd orbital population gives rise to $> 10^8$-fold variation in self-exchange rate constants. In systems with negligible inner-shell barriers, size variations alone can give rise to a 10^5-fold variation in bimolecular exchange rate. The dependence of electron-transfer rate on the separation of the redox sites arises from the dependence of both electronic and nuclear factors on distance. The dependence of the nuclear factor (through λ_{out}) on distance may be experimentally evaluated in binuclear species in which

the redox sites are bound at known distance: MMCT band energies in selected systems give λ_{out} directly, as can the driving-force corrected temperature dependence of the thermal rate constant, or the free-energy dependence of the rate at fixed distance. It is concluded that intramolecular electron-transfer rates may vary a thousand-fold over the distance range 9-20 Å as a consequence of changes in the nuclear factor (λ_{out}) alone, thus posing a serious complication in the investigation of the attenuation of the electronic factor with distance. The decays of many MLCT excited states via intramolecular electron transfer lie in the inverted free-energy region. Thus their decay rates increase when λ_{out} is increased by increasing solvent polarity or diminishing molecular size. The results considered here underscore the importance of accurate experimental or computational evaluation of λ_{out}.

Acknowledgement

This research was carried out at Brookhaven National Laboratory under contract DE-AC02-76CH00016 with the U. S. Department of Energy and supported by its Division of Chemical Sciences, Office of Basic Energy Sciences.

REFERENCES

1. R. A. Marcus, Ann. Rev. Phys. Chem. 15, 155-196 (1964).
2. R. A. Marcus, Disc. Faraday Soc. 29, 21-31 (1960).
3. D. DeVault, Quart. Rev. Biophys. 13, 387-564 (1980).
4. N. Sutin, Acc. Chem. Res. 15, 275-282 (1982).
5. N. Sutin, Prog. Inorg. Chem. 30, 441-498 (1983).
6. M. D. Newton and N. Sutin, Ann. Rev. Phys. Chem. 35, 437-480 (1984).
7. R. A. Marcus and N. Sutin, Biochim. Biophys. Acta 811, 265-322 (1985).
8. R. A. Marcus, J. Chem. Phys. 43, 679-701 (1965).
9. B. S. Brunschwig, S. Ehrenson and N. Sutin, J. Phys. Chem. 90, 3657-3668 (1986).
10. J. Ulstrup and J. Jortner, J. Phys. Chem. 63, 4358-4368 (1975).
11. J. Jortner, J. Chem. Phys. 64, 4860-4867 (1976).
12. B. S. Brunschwig and N. Sutin, Comments Inorg. Chem. 6, 209-235 (1987).
13. R. A. Marcus and P. Siders, J. Phys. Chem. 86, 622-630 (1982).
14. B. S. Brunschwig, S. Ehrenson and N. Sutin, J. Am. Chem. Soc. 106, 6858-6859 (1984).
15. N. Sutin, Supramolecular Photochemistry, pp. 73-86, V. Balzani, Ed., D. Reidel, Holland (1987).
16. B. S. Brunschwig, C. Creutz, D. H. Macartney, T.-K. Sham and N. Sutin, Faraday Disc. Chem. Soc. 74, 113-127 (1982).
17. D. J. Szalda, D. H. Macartney and N. Sutin, Inorg. Chem. 23, 3473-3479 (1984).
18. B. S. Brunschwig and N. Sutin, J. Am. Chem. Soc. 100, 7568-7577 (1978), and references cited therein.
19. G. M. Brown and N. Sutin, J. Am. Chem. Soc. 101, 883-892 (1979).
20. N. S. Hush, Prog. Inorg. Chem. 8, 391-444 (1967).
21. C. Creutz, Prog. Inorg. Chem. 30, 1-73 (1983).
22. S. S. Isied, A. Vassilian, R. H. Magnuson and H. A. Schwarz, J. Am. Chem. Soc. 107, 7432-7438 (1986).
23. S. S. Isied, A. Vasillian, J. F. Wishart, C. Creutz, H. A. Schwarz and N. Sutin, J. Am. Chem. Soc. 110, 635-637 (1988).
24. R. A. Marcus and N. Sutin, Comments Inorg. Chem. 3, 119-133 (1986).
25. H. Elias, M. H. Chou and J. R. Winkler, J. Am. Chem. Soc. 110, 429-434 (1988).
26. K. M. Yocom, J. B. Shelton, J. R. Shelton, W. A. Schroeder, G. Worosila, S. S. Isied, E. Bordignon and H. B. Gray, Proc. Natl. Acad. Sci., USA 79, 7052-7055 (1982).
27. T. J. Meade, H. B. Gray and J. R. Winkler, work in progress.
28. A. W. Axup, M. Albin, S. L. Mayo, R. J. Crutchley and H. B. Gray, J. Am. Chem. Soc. 110, 435-439 (1988).
29. J. L. Karas, C. M. Lieber and H. B. Gray, J. Am. Chem. Soc. 110, 599-600 (1988).
30. H. B. Gray, work in progress.
31. B. S. Brunschwig, S. Ehrenson and N. Sutin, J. Phys. Chem. 91, 4714-4723 (1987).
32. A. Juris, V. Balzani, F. Barigelletti, S. Campagna, P. Belser and A. von Zelewsky, Coord. Chem. Rev. 84, 85-277 (1988) and references cited therein.
33. J. V. Caspar and T. J. Meyer, J. Am. Chem. Soc. 105, 5583-5590 (1983); Inorg. Chem. 22, 2444-2453 (1983).
34. E. M. Kober, B. P. Sullivan and T. J. Meyer, Inorg. Chem. 23, 2098-2104 (1984).
35. E. M. Kober, J. V. Caspar, R. S. Lumpkin and T. J. Meyer, J. Phys. Chem. 90, 3722-3734 (1986).
36. J. V. Caspar, T. D. Westmoreland, G. H. Allen, P. G. Bradley, T. J. Meyer and W. H. Woodruff, J. Am. Chem. Soc. 106, 3492-3500 (1984).
37. T. J. Meyer, Pure Appl. Chem. 58, 1193-1206 (1986).
38. C. Creutz, unpublished work.
39. J. R. Winkler, T. L. Netzel, C. Creutz and N. Sutin, J. Am. Chem. Soc. 109, 2381-2392 (1987).